Tunnelling and Underground Space Technology 72 (2018) 84–96

Contents lists available at ScienceDirect

Tunnelling and Underground Space Technology

journal homepage: www.elsevier.com/locate/tust

Evaluation of the wall deflections of a deep excavation in Central Jakarta using three-dimensional modeling

Bin-Chen Benson Hsiung[a,*], Kuo-Hsin Yang[b], Wahyuning Aila[c], Louis Ge[b]

[a] Department of Civil Engineering, National Kaohsiung University of Applied Sciences, 415, Chen Kung Road, Kaohsiung 807, Taiwan
[b] Department of Civil Engineering, National Taiwan University, No. 1, Sec. 4, Roosevelt Road, Taipei 10617, Taiwan
[c] Department of Civil and Construction Engineering, National Taiwan University of Science and Technology (Taiwan Tech), 43, Sec. 4, Keelung Rd., Taipei 106, Taiwan

ARTICLE INFO

Keywords:
Deep excavation
Central Jakarta
Clay
Wall deflection
Three-dimensional effect
Plane strain ratio (PSR)

ABSTRACT

This paper presents a case study and numerical simulations regarding a large-scale deep excavation in Central Jakarta, Indonesia, and its three-dimensional (3D) effects on wall deformation. The soil profile in Central Jakarta is generally soft to firm alluvial clay overlying stiff to hard alluvial and diluvial clay. In this study, the geotechnical engineering properties of soil (i.e., undrained shear strength and modulus) were established using data from a site investigation, in situ and laboratory tests, and empirical correlations with standard penetration numbers (SPT-N). A summary of simplified soil input properties for subsurface soil in Central Jakarta was provided. To analyze the deep excavation case, a 3D finite element model was developed by considering a top-down construction method, a supporting system of concrete slabs, and the influence of the soil modulus. The numerical results indicated that the hardening soil model with the soil modulus obtained from in situ pressuremeter tests yields reasonable predictions for excavation-induced wall deformation. The applicability of 3D finite element analyses to capturing the 3D corner effect on the wall deformation was validated. According to the parametric study, the plane strain ratio (PSR) was determined for the excavations in Jakarta clay. Compared with the PSR developed for Taipei clay, this study revealed that the PSR value was influenced not only by the 3D corner effect but also by the stiffness of the subsurface soil. In addition to PSR, the wall deflection path was also affected by the 3D corner effect and soil modulus.

1. Introduction

Jakarta is the capital and largest city of the Republic of Indonesia. With a population of 10 million and limited urban public transport services, additional underground space is required for transportation nerworks, for which deep excavation is crucial. Many studies have evaluated the effect of deep excavations on the behavior of walls (Clough and O'Rourke, 1990; Ou et al., 1996, 2000; Ou, 2006; Kung et al., 2007; Lin and Woo, 2007; Hsiung, 2009; Schweiger, 2009; Wang et al., 2010; Likitlersuang et al., 2013; Khoiri and Ou, 2013; Finno et al., 2015; Orazalin et al., 2015; Hsieh et al., 2015; Hsiung et al., 2016), but limited studies have reported excavation cases in Jakarta, Indonesia. Furthermore, explorations of soil properties are limited, and few of the large-scale deep excavations in the city have been well documented. Most of the available information is documented mainly in the local language. All of these factors increase the difficulty of studying deep excavation in Jakarta area.

In engineering practice, two-dimensional (2D) finite element (FE) analysis is generally performed because of time and budget limitations, although three-dimensional (3D) FE analysis has already been used to study 3D wall behavior. The concept of plane strain ratio (PSR), proposed by Ou et al. (2006), is used to accurately quantify 3D excavation-induced behaviors from the output of 2D FE analysis. The PSR is the ratio of the maximum wall deformation of a section of a wall at a distance *d* from the corner to the maximum wall deformation of the section under plane strain conditions. The PSR was adopted in this study to quantify the 3D wall behavior of an excavation in clay in Central Jakarta.

This paper presents a unique and well-documented case of a large-scale deep excavation in clay in Central Jakarta. The excavation was nearly completely embedded in thick layers of clay. Detailed background information regarding the subsurface soil conditions, in situ and laboratory soil tests, construction sequences, and monitoring data are introduced and discussed. The input soil parameters were estimated and interpreted from in situ and laboratory triaxial tests. Moreover, the determined soil parameters were compared with the estimated values using several empirical correlations with the standard penetration number (SPT-N) to confirm the reliability of the parameters that were

* Corresponding author.
E-mail addresses: benson.hsiung@gmail.com (B.-C.B. Hsiung), khyang@ntu.edu.tw (K.-H. Yang), wahyuningaila@gmail.com (W. Aila), louisge@ntu.edu.tw (L. Ge).

https://doi.org/10.1016/j.tust.2017.11.013
Received 1 October 2016; Received in revised form 18 October 2017; Accepted 1 November 2017

used in the analyses. A 3D FE analysis was then conducted to model the selected deep excavation in Central Jakarta and to verify the applicability of 3D FE models in predicting a 3D excavation-induced wall displacement (also known as a 3D corner effect). The results of the numerical analysis and field observations were compared and discussed. Finally, a PSR chart for excavations in Central Jakarta was developed through a series of parametric studies with several excavation aspect ratios. The proposed PSR chart provided an alternative approach to transfer the wall displacement from a 2D analysis to one considering the 3D corner effect. Thus it enabled a practical design (typically 2D) to account for the 3D effects of an excavation on wall deformation.

2. Project background

A deep excavation in Central Jakarta, Indonesia was selected for the case study and numerical simulation. The length of the excavation was 430 m and the width varied from 22 to 30 m in different sections. The construction was performed using a top-down method with five excavation stages, supported by four-level reinforced concrete slabs with various thicknesses. The maximum excavation depth was 18.9 m in the final excavation stage. The excavated pit was retained using a 1.0-m thick and 24.1-m deep diaphragm wall. Figs. 1 and 2 show the cross section and photograph of the excavation, respectively.

To increase the stiffness of the retaining wall system, 414 × 405 × 18 × 28 steel H-beams were installed as kingposts in the middle of the excavation area at 3.0-m intervals. The kingposts bore the weight of concrete floor slabs and the possible lateral loading from the diaphragm wall, which was transferred to the slabs. The H-beams were inserted 4.0 m into bored piles with a diameter of 1.0 m and an embedded length of 14.5 m.

The diaphragm wall and kingposts were constructed before the soil was excavated to ground level (GL) − 1.5 m. In the next phase, a deck slab with a thickness of 0.4 m was installed. The second excavation stage involved removing the soil to GL − 5.08 m and then constructing a top slab at GL − 4.18 m. Subsequently, the soil was excavated to GL − 11.18 m and a middle slab with a thickness of 0.4 m was placed at GL − 10.48 m. The fourth and fifth excavation stages were conducted similarly. In the final construction phase, the bottom slab with a thickness of 1.0 m was installed at GL − 18.13 m. Table 1 details the construction phases and sequences of the excavation.

3. Instrumentation and observations

To monitor the performance of the diaphragm wall during construction, several monitoring instruments were installed around the excavation site, including inclinometers, surface settlement points, observation wells, rebar stress transducers, and kingpost strain gauges. All monitoring data were carefully reviewed and only reliable and representative data were selected for further analysis and discussion. Inclinometers were installed at several cross sections of the site to measure the lateral movement of the diaphragm wall. The inclinometers were installed on the left and right sides of the diaphragm wall. Fig. 3 displays the locations of the inclinometers at five

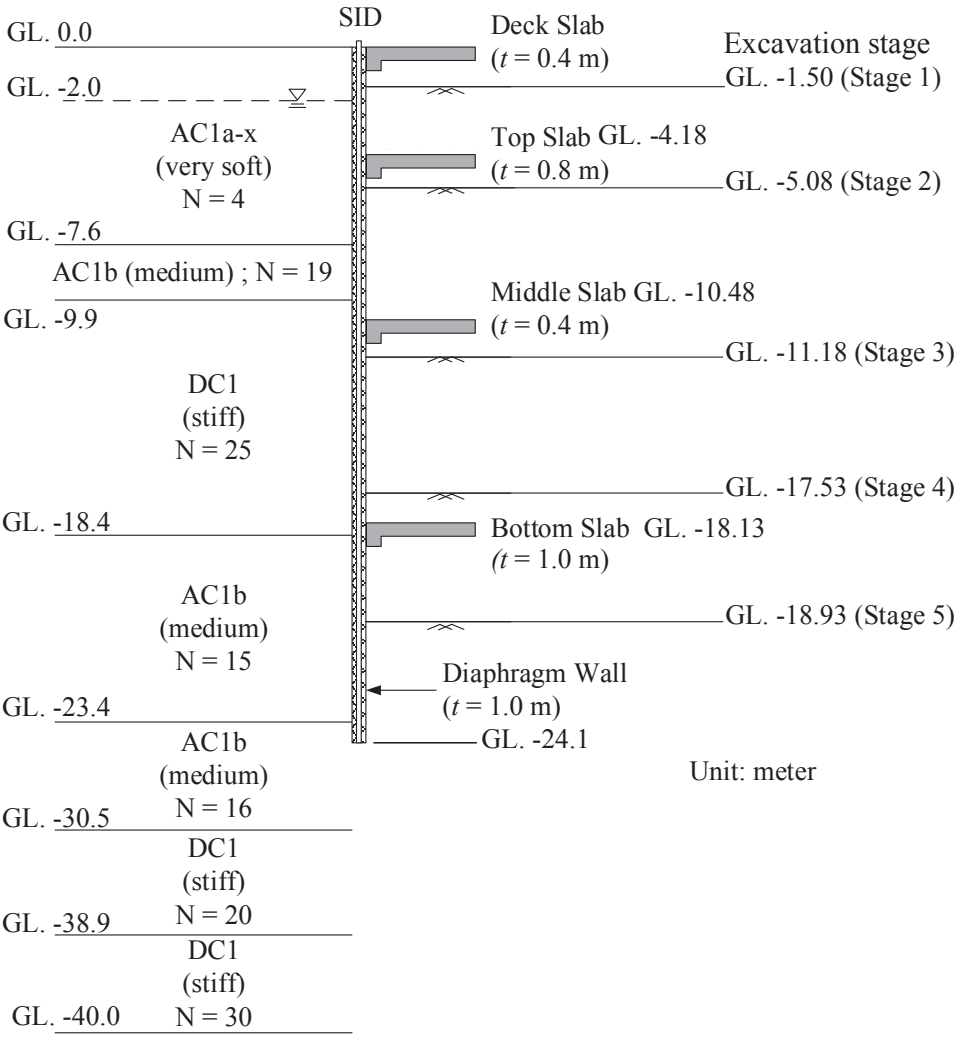

Fig. 1. Cross section and soil profile of the excavation.

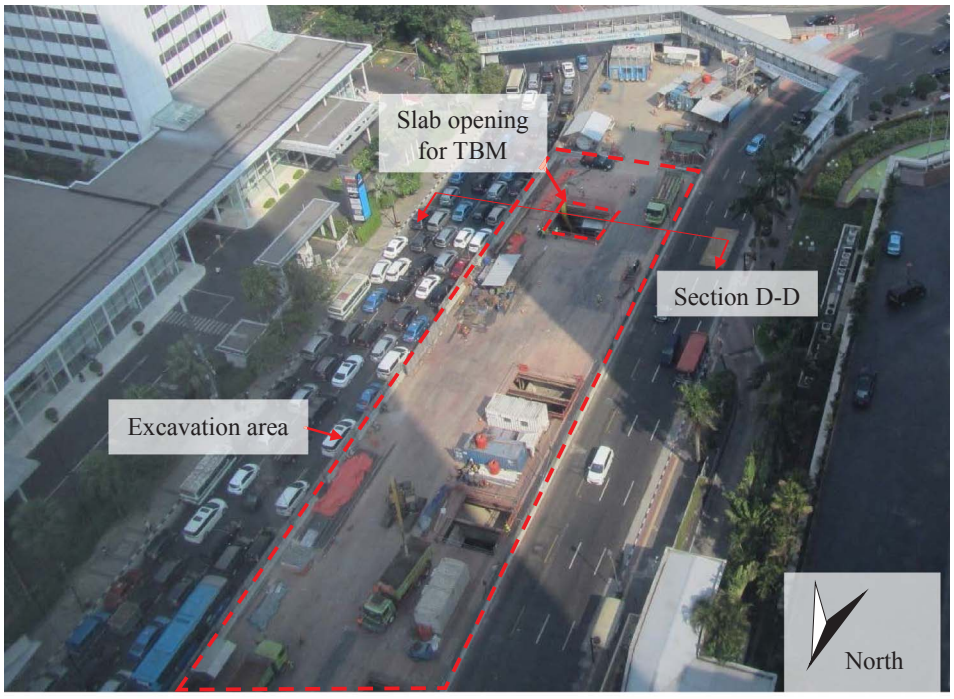

(a)

(b)

Fig. 2. Photo of the excavation site: (a) overview; (b) close view.

Table 1
Construction phases and sequences of the excavation.

Phases	Construction sequences	Elapsed days
1	Diaphragm wall installation	101
2	1st excavations to the depth of GL. −1.5 m	18
3	Deck slab installation at ground level (slab thickness, t = 0.4 m)	20
4	2nd excavation to the depth of GL. −5.08 m	30
5	Top slab construction at GL. −4.18 m (slab thickness, t = 0.8 m)	14
6	3rd excavation to the depth of GL. −11.18 m	22
7	Middle slab construction at GL. −10.48 m (slab thickness, t = 0.4 m)	20
8	4th excavation to the depth of GL. −17.53 m	28
9	5th excavation to the depth of GL. −18.93 m	28
10	Bottom slab construction at GL. −18.13 m (slab thickness, t = 1.0 m)	21

monitoring sections. Among these five sections, wall deflection data from Sections E-E, D-D, and H-H were used for further discussion and analysis. Sections G-G and F-F were not analyzed because the excavation depth was not symmetric at both sides. The east side of the diaphragm wall in Section F-F was installed with knock-out panels and opening for the entrance to the underground station.

Inclinometer readings are reliable when the tip of the inclinometer is properly embedded into a stable stratum, thereby preventing the inclinometer tip from moving with the diaphragm wall (Hsieh et al., 2015). In general, if the toe of the inclinometer does not move during excavation, the wall movement can be measured accurately. Unfortunately, in this study, the installed inclinometers either had the same penetration depth as that of the diaphragm wall or had toes that stopped above the bottom of the wall. This circumstance can cause inaccurate measurements of diaphragm wall movements because of the comparatively short penetration depth. Thus, inclinometer readings must be corrected to account for toe movement.

Various methods have been proposed for the correction of inclinometer readings to address toe movement. Hwang and Moh (2007)

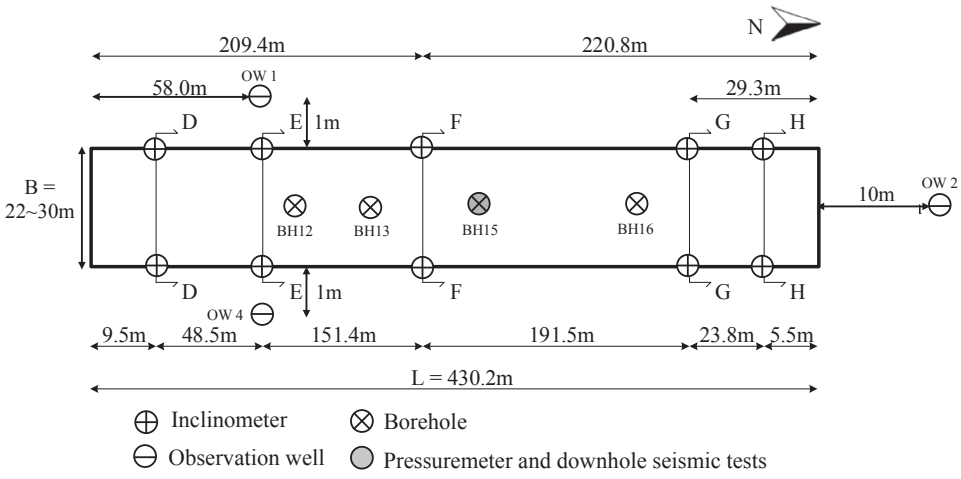

Fig. 3. Plan view of the excavation, inclinometer sections, and location of instrumentation (not to scale).

and Hsiung and Hwang (2009) have suggested that inclinometer readings could be corrected by referring to the lateral movement at the B1F level during each excavation stage. This method assumes that the increment of the inclinometer reading at the reference point (i.e., the B1F level) for each excavation stage has a positive value, indicating that the wall at the reference point always moves forward (toward the excavation side). If the inclinometer is subjected to the toe movement, the increment of the inclinometer reading at the reference point may reveal a negative value, indicating that the wall at the reference point moved toward the retained soil side. Under these conditions at any excavation stage, the entire wall deflection curve must be shifted in parallel so that the wall deflection at the reference point can return to the same magnitude at previous excavation stage. Fig. 4 shows an example of lateral wall deformation before and after correction.

For observations from the construction site, attention was also paid to changes in the water levels outside the excavation. Fig. 5 presents changes in water levels at three observation wells (OWs) outside the excavation. All OWs exhibited water level rises from early January to mid-February 2015, possibly because of heavy rainfall during the monsoon season. Because OW2 was located farther from the excavation (Fig. 3), the water level remained at approximately 2 m below the surface level during the entire construction period. However, the water levels observed at the other two wells dropped between 1 and 2 m during the excavation and rose after its completion. Although OW1 and OW4 were located outside the excavation and no pumping was conducted, their changes in water levels may be connected with a water head change caused by natural seepage or soil stress relief under the influence of the excavation.

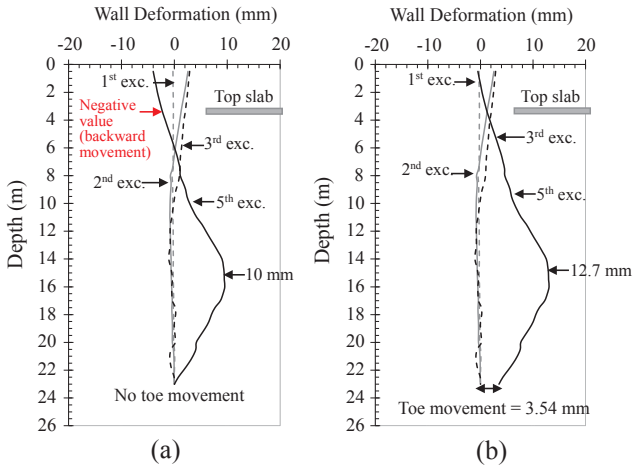

Fig. 4. Example of wall deformation correction: (a) original (before correction); (b) after correction.

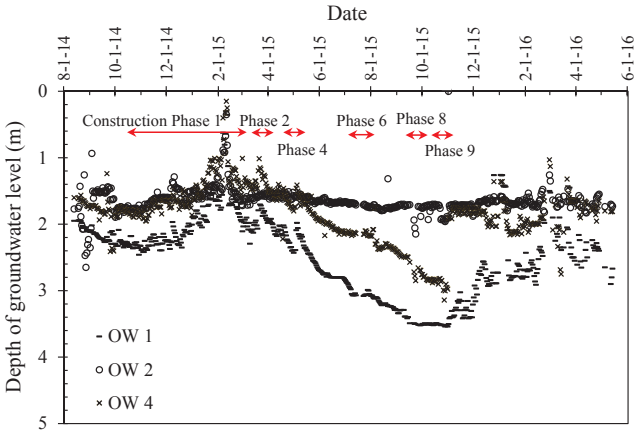

Fig. 5. Monitoring of groundwater level outside the excavation at each construction phase (arrows indicate the construction period).

Surface settlement caused by the excavation was measured using a limited number of settlement nails (approximately 40) on the surface located between 3 and 20 m from the excavation. The excavation caused up to 15 mm of surface settlement. The settlement curves were not presented in this paper because the quality of some settlement nails was degraded or damaged by the heavy traffic (Fig. 2a).

4. Site investigation

4.1. In situ and laboratory soil tests

A geotechnical investigation involving in situ and laboratory tests was conducted to determine the soil properties at the excavation project. The site investigation work included 10 boreholes and standard penetration tests (SPTs) were performed at intervals of 1–2 m. In situ tests including cone penetration tests (CPTs), pressuremeter tests (PMTs), downhole seismic logging tests, and permeability tests were conducted. Figs. 6 and 7 present profiles of the site investigation results from the selected boreholes.

The borehole results from the site investigation appeared to correlate with the local geological settings; the subsurface soil contained mostly clay, silty clay, and clayey silt. Notably, as shown in Fig. 6b and c, although the subsurface soil is mainly classified as clay soil, the sand content could be up to 50% almost covering the entire excavation depth. In general, the stratigraphic profile consisted of soft to firm alluvial clay (AC) overlying stiff to hard AC and diluvial clay (DC). On the basis of the soil consistency, the AC and DC were divided

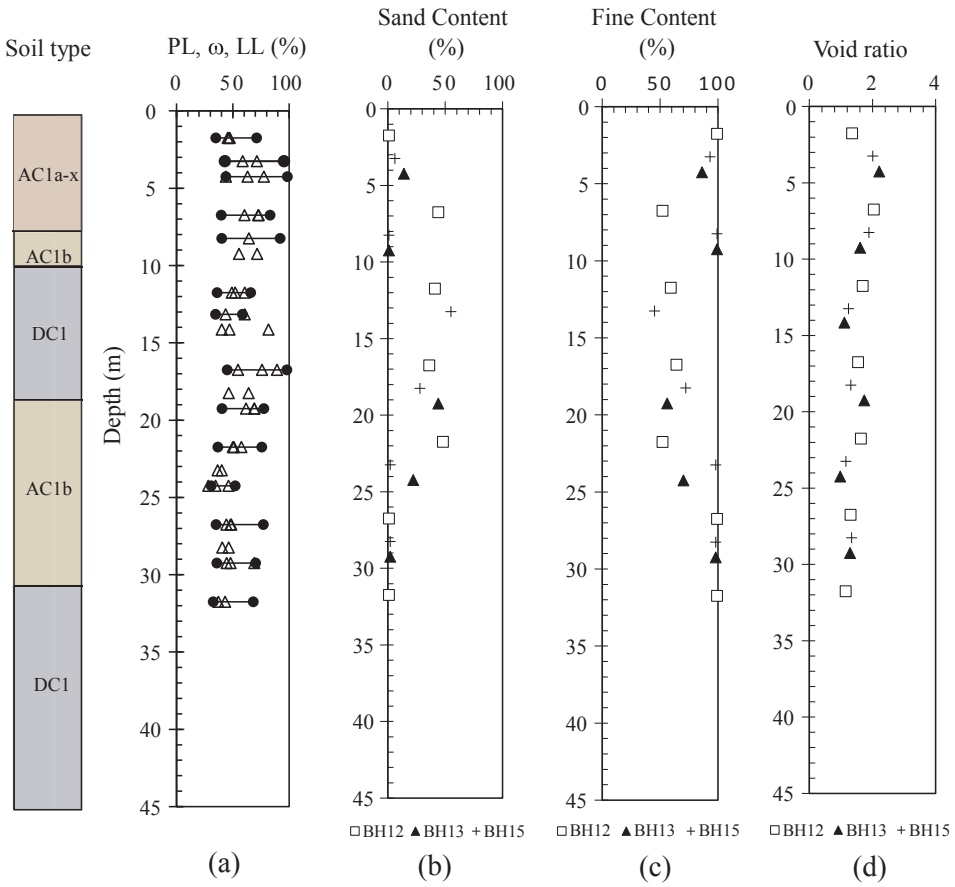

Fig. 6. Profiles of subsurface soil information: (a) water content, plastic limit and liquid limit; (b) sand content; (c) fines content; and (d) void ratio.

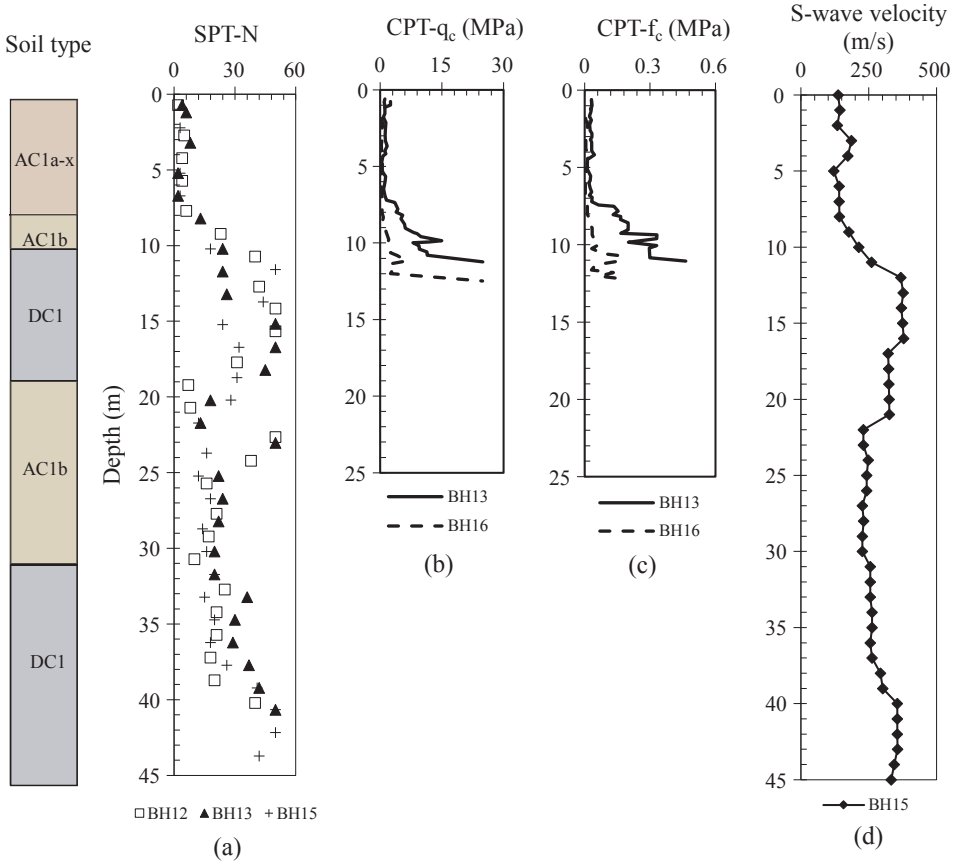

Fig. 7. Profiles of in-situ test information: (a) SPT-N; (b) CPT-cone resistance; (c) CPT-friction resistance; and (d) shear wave velocity.

Table 2
Input soil parameters in HS model.

Depth (m)	Soil type	Consistency	Average SPT-*N*	γ	S_u	K_o	E_{50} (kPa)			E_{50}^{ref} (kPa)		
				(kN/m^3)	(kN/m^2)		2800N	4000N	PMT	2800N	4000N	PMT
0.0–7.6	AC1a-x	Very soft	4	15.5	24	0.58	11,200	16,000	66,822	9744	13,920	58,135
7.6–9.9	AC1b	Medium	19	17	114	0.58	53,200	76,000	70,937	46,284	66,120	61,715
9.9–18.4	DC1	Stiff	25	18	150	0.58	70,000	100,000	75,452	60,900	87,000	65,643
18.4–23.4	AC1b	Medium	15	17	90	0.47	42,000	60,000	81,075	36,540	52,200	70,535
23.4–30.5	AC1b	Medium	16	17	96	0.47	44,800	64,000	86,106	38,976	55,680	74,912
30.5–38.9	DC1	Stiff	20	18	120	0.47	56,000	80,000	92,562	48,720	69,600	80,528
38.9–40.0	DC1	Stiff	30	18	180	0.47	84,000	120,000	98,310	73,080	104,400	85,529

Note: $E_{oed}^{ref} = 0.7E_{50}^{ref}$; $E_{ur}^{ref} = 3E_{50}^{ref}$,; $m = 1.0$; $R_f = 0.9$; $\nu' = 0.3$; and $\nu_{ur} = 0.2$.

into several sublayers, including AC1a-x, AC1b, and DC1. The soil unit weight varied between 15 and 18 kN/m^3. Fig. 1 displays the subsurface soil profile of the excavation site. Table 2 lists a simplified summary of the anticipated soil stratigraphy.

Fig. 6a shows the relationships of the natural water content (ω) and the Atterberg limit test results with depth. The natural water content was in the range of 28.19–89.26% and was generally close to or higher than the plastic limit, with a liquidity index (LI) of 0.05–0.65. A gradual decrease in the LI with depth was also noticed in this excavation, suggesting that shear strength may increase with depth. A high void ratio was associated with the high water content (Fig. 6d), especially for the soil layer occupying top 10 m.

SPTs were conducted along with the boring operation at intervals of 1–2 m. Fig. 7a shows the SPT-N profile collected from three on-site boreholes (BH12, BH13 and BH15). The soil strata were separated predominantly according to their SPT-N values and their stratigraphic position in the geological profile. The SPT results suggested that the AC1a and AC1b layers were separated; specifically, the AC material from near the ground surface to a depth of 8 m typically exhibited SPT-N values of 1–8. In some areas, a very soft to soft material was observed in the upper soil layer, which typically exhibited a low SPT-N value of 0–4. Such material, which exhibits soil stiffness and strength substantially lower than those of AC1a, is referred to as AC1a-x. The DC1 at the middle and bottom of the soil profile typically had SPT-N values of 20–50. Table 2 summarizes the average SPT-N values for each soil layer.

Fig. 7b and c shows tip resistance (q_c) and skin friction (f_s) according to the CPT results. The q_c was generally low for the top 7 m of soil, but it gradually increased with depth until reaching nearly 30 MPa at approximately 11 m below ground surface. The CPT results (q_c and f_s) exhibited a trend similar to those of the SPT-N values. Because of limited machine capacity, the maximum effective depth of the CPTs was limited to 13 m; the tests could reach the maximum excavation depth of 18.6 m. Additionally, because the CPT cone was not equipped with a piezometer (only CPT instead of CPTU), the porewater pressure during the test could not be measured. Because of the aforementioned reasons, the CPT data was insufficient to establish completed profiles of the soil modulus and shear strength properties of the ground.

Downhole seismic logging tests were carried out on site to measure the shear wave velocity of soil to a depth of 45 m. The measured maximum shear wave velocity is approximately of 400 m/s at the depth of 10–20 m (Fig. 7d). In situ permeability tests, by means of the falling-head method, have been performed in selected boreholes (BH15-17). After firstly measuring the initial level of the ground water table, then the casing is filled with water until reaching the top of the casing pipe. The water drop-down is measured at certain time intervals until reaching the stable or up to the first initial water level. The permeability test results indicate that the hydraulic conductivity of the in-situ soil in the studied section is in the range of 3×10^{-8} to 7×10^{-8} m/s.

Disturbed and undisturbed samples (collected in Shelby tubes) were obtained for laboratory tests, including soil index property tests (Fig. 6), chemical tests, triaxial unconfined compression (UC) tests, and triaxial consolidated undrained (CU) tests with pore pressure measurements. The data obtained from the in situ and laboratory tests were subsequently applied to determine the soil modulus and shear strength properties.

4.2. Soil modulus and shear strength properties

The undrained shear strength (S_u) of the clay was obtained from triaxial UC tests and validated through several empirical methods for estimating the S_u of the clay. A common empirical method proposed by Houston and Mitchell (1969) and Muir Wood (1983) correlates S_u with the LI. The empirical equation proposed by Muir Wood (1983) is as follows.

$$S_u = 170 \times e^{-4.6LI} \quad \text{(kPa)} \tag{1}$$

Another common empirical method discussed in Hettiarachchi and Brown (2009) correlates S_u with the SPT-N. The empirical equation proposed by Kulhawy and Mayne (1990) is as follows.

$$S_u = 6 \times N \quad \text{(kPa)} \tag{2}$$

Fig. 8 compares the S_u profile calculated from LI (the green shaded area), the SPT-N (red dash line), and the triaxial UC test results (hollow circles). The S_u values obtained from these three methods display a

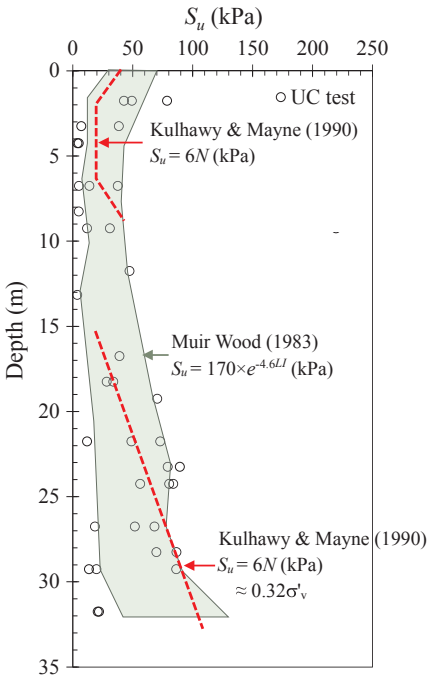

Fig. 8. Undrained shear strength with depth.

similar trend. For depths of 15–30 m, the S_u value increased linearly with depth and could be approximated as $0.32\sigma'_v$ (where σ'_v is the effective overburden pressure). For simplicity, the S_u of the soil for the numerical simulation was determined using Eq. (2) and the results are listed in Table 2.

Regarding effective soil shear strength of clay, few high-quality reliable CU tests were delivered, and the effective friction angle of the soil was in the range of 30° to 34°. However, the number of CU tests was insufficient to represent a complete profile of effective shear strength parameters for numerical analyses and comparison. These effective friction angle values were only applied to estimate the K_0 values for generating initial stress in the numerical simulation. The K_0 values was defined by using equations from Jaky (1944) for normally consolidated soils and from Mayne and Kulhawy (1982) for overconsolidated soils, as shown in Eq. (3).

$$K_{0(NC)} = 1-\sin\phi' \tag{3a}$$

$$K_{0(OC)} = (1-\sin\phi') \times OCR^{(\sin\phi')} \tag{3b}$$

where $K_{0(NC)}$ and $K_{0(OC)}$ are the at-rest earth pressure coefficient for normally consolidated and overconsolidated soils, respectively, ϕ' is the effective friction angle, and OCR is the overconsolidation ratio. The investigated clay at depth of approximately above 15 m is overconsolidated and below 15 can be treated as normally consolidated. The average $OCR = 1.5$ was input for the top three soil layers to estimate their $K_{0(OC)}$ values. Table 2 summarizes the estimated K_0 values.

The soil modulus (E) is a key parameter for estimating soil deformation characteristics. The soil modulus can typically be directly determined through triaxial or oedometer tests in a laboratory and from PMT in the field, or estimated indirectly from SPT or CPT. As suggested by Hsiung (2009) and Yong (2015), the soil modulus for sand is estimated as $E = 2000\,N$ (kPa) and that for clay as $E = 4000\,N$ (kPa). In addition, the Architectural Institute of Japan (2001) suggested that $E = 2800\,N$ (kPa) can be applied for all soils. The soil modulus measured from PMT was expected to be close to the initial soil modulus (E_i). For comparison, the measurements were converted to the soil modulus at 50% stress level (E_{50}) by using Eq. (4), assuming a hyperbolic curve for the stress–strain relationship.

$$E_{50} = E_i \frac{2-R_f}{2} \tag{4}$$

where E_i is the initial soil modulus and R_f is the failure ratio, which is assumed to be 0.9 for clay. Fig. 9 presents a comparison of E_{50} versus depth with various approaches and tests. The E_{50} values determined from PMT appear to become linearly associated with depth. This observation is consistent with the findings of Hsiung et al. (2016), who reported that a linear relationship exists between soil stiffness and depth. The linear regression line for E_{50} obtained from PMTs is expressed as follows.

$$E_{50} = 833(z + 76)\ \text{(kPa)} \tag{5}$$

where z is the soil depth in meters. The E_{50} values obtained from the CU tests tend to be at the lower bound of the E_{50} values compared to those determined using PMT and estimated from SPT (Fig. 9). The low E_{50} values may have been attributable to the sample disturbance and the quality of the soil sample. Table 2 summarizes the E_{50} values determined from PMT (Eq. (5)) and estimated from empirical correlations with SPT-N, as proposed by the Architectural Institute of Japan (2001) and Yong (2015).

5. Finite element analysis

5.1. Numerical model

A 3D FE analysis, also called a benchmark analysis, was conducted to examine the performance of the excavation in this study. The commercial FE software PLAXIS 3D was used as a numerical tool for the 3D analyses. Fig. 10 shows the 3D FE model of the benchmark analysis. The FE model comprised 19,330 10-node tetrahedral elements with a total of 31,322 nodes. The dimensions of the FE model were 182 m × 100 m × 60 m. A half excavation area with a length of 40 m was modeled using a symmetric model. Hence, the model total length of the excavation was 80 m. Although the actual full length of the excavation was 430 m, only 80 m of the excavation length was considered in this model. This was because the influence of corner effects becomes insignificant once the distance is 30 m from the corner. At distances of 30 m away from the corner, the wall is essentially under plane strain conditions and the wall deformation remains nearly constant (Ou, 2006; Ou et al., 1996; Hsiung et al., 2016). This claim is demonstrated and discussed in Section 6.1. Additionally, shortening the excavation length reduces the size of the 3D model, saving computational time and cost without affecting the numerical results.

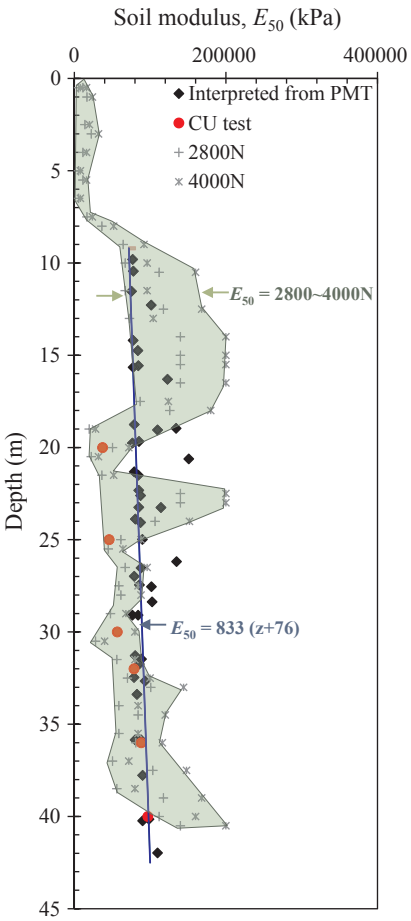

Fig. 9. Comparisons of soil modulus measured from PMT, triaxial tests and those estimated by various empirical approaches.

Ten construction phases were modeled as listed in Table 1. In addition to modeling the 10 construction phases, the groundwater table was initial set 2.0 m below the ground surface and lowered to 1.0 m below excavation surface at each excavation stage. The distance from the lateral boundaries of the model to the retaining wall was 80 m, which was approximately four times the excavation depth. Standard fixed conditions were applied to the FE model; horizontal movement was restrained at the lateral boundaries, and both horizontal and vertical movements were restrained at the bottom boundary of the model. The soil model, structural elements (diaphragm walls and floor slabs), and soil-structure interface elements are discussed in the following section. Finally, a greenfield analysis was performed so that potential loads from traffic on the main road were not considered.

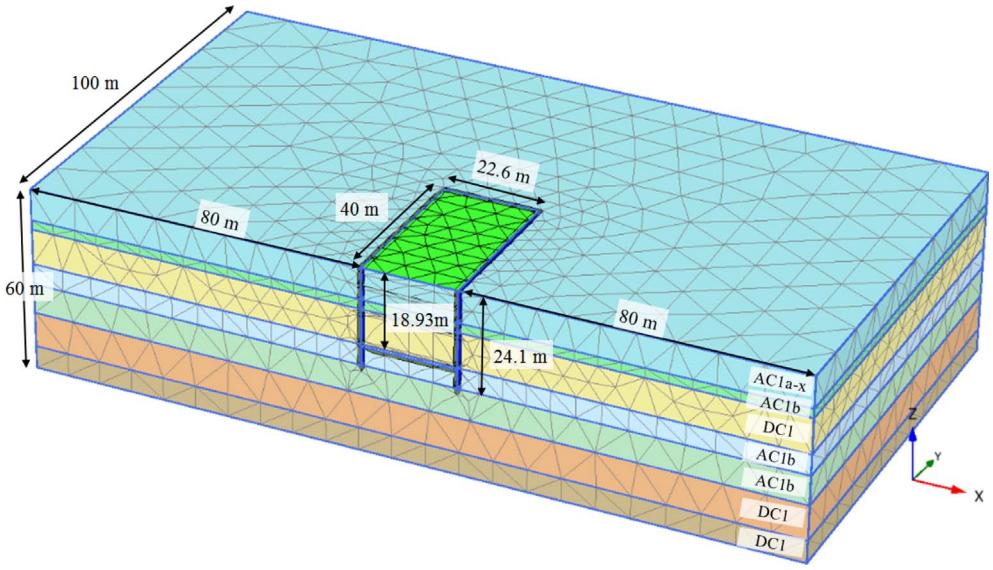

Fig. 10. 3D Finite element model of benchmark analysis.

5.2. Soil model and input properties

In this study, a hardening soil (HS) model was coded in PLAXIS and adopted for the numerical simulation. Table 2 lists the input soil parameters in the HS model for the FE analyses. The effective stress analysis under undrained conditions was performed to model the short-term undrained conditions of the clay during excavation. The assumption of soil undrained conditions can be justified by the measured low soil permeability, as reported previously. Furthermore, the real construction revealed that no pumping water out the excavation area was required through the whole excavation process (typically dewatering required for soils with high to medium permeability during construction), suggesting that the soil in the studied section remained undrained conditions.

Two undrained functions, namely *Undrained* (*A*) and *Undrained* (*B*), were specified in PLAXIS: *Undrained* (*A*) requires effective stress parameters for both soil modulus and shear strength, whereas *Undrained* (*B*) uses the effective soil modulus and undrained soil shear strength. As discussed earlier, because a limited number of high-quality CU tests were conducted, a representative profile of effective shear strength parameters was not obtained. Therefore, the *Undrained* (*B*) function, using the effective soil modulus and undrained soil shear strength, was selected for analysis. The determination of the undrained soil shear strength was discussed in Section 4.2.

The numerical simulations were performed using three soil moduli determined from PMT and estimated using empirical correlations with the SPT-N, as proposed by the Architectural Institute of Japan (2001) and Yong (2015). The drained soil modulus in Fig. 9 was converted to the effective soil modulus E'_{50} using Eq. (6), which is based on elasticity theory.

$$E'_{50} = E_{50}\frac{2(1+\nu')}{3} \tag{6}$$

where E'_{50} and E_{50} are the drained and undrained soil moduli at the 50% stress level and ν' is the effective Poisson's ratio, assumed to be 0.3 for clay. Eq. (6) can be further simplified into $E'_{50} = 0.867E_{50}$. As noted in the PLAXIS manual, when selecting *Undrained* (*B*), the soil modulus in HS model becomes stress-independent. Hence, E'_{50} can be used directly as the drained reference soil modulus (E_{50}^{ref}) in the HS model. However, the stress dependency of the soil modulus was still modeled by manually inputting various soil modulus values for soil layers to consider the change of the soil modulus with depth. Table 2 lists the E_{50}^{ref} values used in the simulation. Unlike the Mohr-Coulomb model, which only has a single soil modulus value, the HS model allows to input separated soil modulus values for differentiating the soil behavior under loading and unloading conditions. According to Lim et al. (2010) and Calvello and Finno (2004), the reference moduli for unloading/reloading and oedometer loading were estimated to be $E_{ur}^{ref} = 3E_{50}^{ref}$ and $E_{oed}^{ref} = 0.7E_{50}^{ref}$, respectively. Similar procedures were suggested by Surarak et al. (2012) to determine input soil parameters in the HS model. In addition, the sensitivity of each parameter on the wall deformation of an excavation was discussed by Gebreselasse and Kemfert (2005).

5.3. Structural and interface elements and input properties

For the excavation structures, plate elements were used to model the diaphragm wall and floor slab in the numerical model. The diaphragm wall in the model was 1.0 m thick and 24.1 m long as constructed in the field. According to the American Concrete Institute, the Young's modulus of concrete (E_c) can be estimated as follows:

$$E = 4700\sqrt{f'_c}\ \text{(MPa)} \tag{7}$$

where f'_c (MPa) is the standard compressive strength of the concrete. To compensate for the overlapping of unit weight and volume between soils and other materials (e.g., concrete and steel), the soil unit weight should be subtracted from the real unit weight of the concrete or steel materials. According to Ou (2006), the stiffness (*EI*) of a diaphragm wall is usually reduced by approximately 20–40% in an analysis to consider defects and cracks in the concrete; hence, an average reduction factor of 30% was employed. Table 3 lists the input material properties of the diaphragm wall.

According to Ou (2006), the axial stiffness of floor slabs in the top-down construction method must also be reduced by approximately 80%. This is because the compressive strength of the constructed concrete might differ from the design strength; defects and cracks in the

Table 3
Input parameters for diaphragm wall.

Parameter	Symbol	Value	Unit
Compressive strength of concrete	f'_c	21	MPa
Thickness	d	1.0	m
Young's modulus	E	21,700	MPa
Young's modulus 70%	70%E	15,200	MPa
Unit weight	w	6	kN/m^3
Poisson's ratio	ν	0.15	

Table 4
Input parameters for concrete slabs.

Slabs	d (m)	γ (kN/m^3)	ν	80%E (MPa)
Deck slab	0.4	24	0.15	17,400
Top slab	0.8	24	0.15	17,400
Middle slab	0.4	24	0.15	17,400
Bottom slab	1.0	24	0.15	17,400

concrete can also be considered through this approach. The slab thickness for each floor level and the parameters for the slabs are listed in Table 4.

Interface elements were employed to simulate the interaction between the soil and structural elements such as the diaphragm wall and bottom concrete slab. The value of the interface reduction factor (R_{inter}) influences both the stiffness and strength of the interface. $R_{inter} = 0.5$, a typical value for the clay and concrete interface, was chosen for the analysis.

5.4. Comparison of measured and predicted wall deformation

Fig. 11 shows comparisons of the measured and predicted wall deformation in Section E-E during various excavation stages. Section E-E is approximately 60 m away from the corner and can be considered as a reference section under plane strain conditions (Fig. 3). As shown in

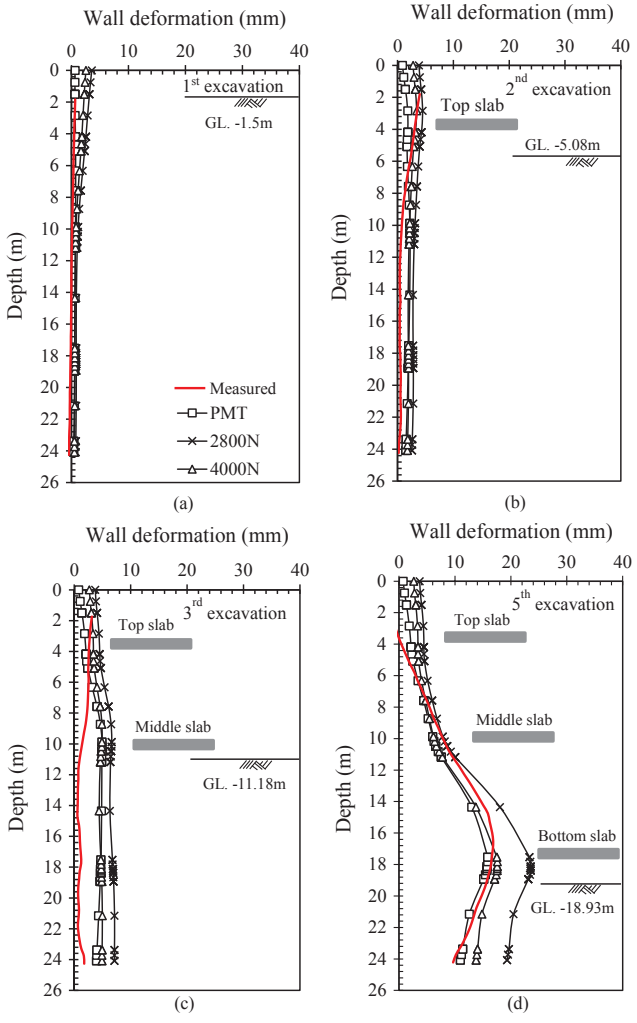

Fig. 11. Comparison of predicted and measured wall displacements at Section E-E at various excavation stages: (a) 1st stage; (b) 2nd stage; (c) 3rd stage; (d) 5th (final excavation) stage.

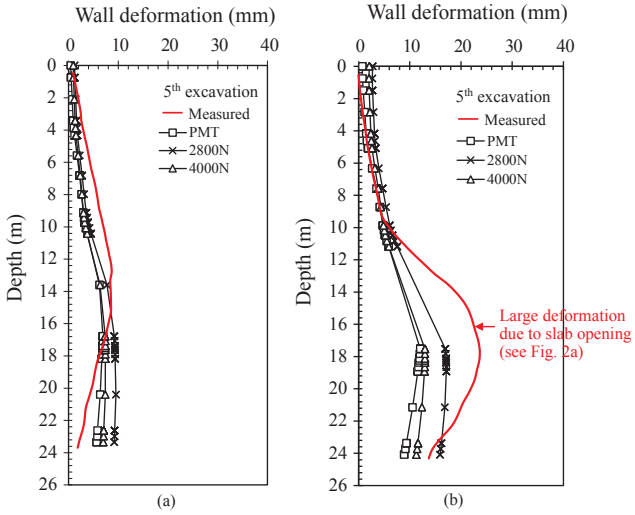

Fig. 12. Comparison of predicted and measured wall displacements at final excavation stage: (a) Section H-H; (b) Section D-D.

Fig. 11, the wall deformation gradually increased from almost no movement during the 1 st excavation stage to 16 mm by the end of the excavation. The maximum wall deformation corresponded to the depth of the final excavation level. The comparison revealed that the predictions that applied E_{50} = PMT were in close agreement with the measured wall deformation, especially at the final excavation stages. The predictions using $E_{50} = 4000\,N$ also matched the measured wall deformation. However, the predictions using $E_{50} = 2800\,N$ overestimated the wall deformation because the lower bound value of the SPT-N correlation was used to estimate the soil modulus in the simulation. Overall, the simulation using E from the PMT appeared to accurately predict the magnitude and shape of the lateral deformation of the diaphragm walls embedded in the clay in Central Jakarta. The accurate predictions also suggested the importance of conducting a detailed site investigation program for obtaining high-quality and reliable parameters for design and analysis.

Fig. 12 shows comparisons of the predicted and measured wall deformation in Sections D-D and H-H at the final excavation stage. Sections D-D and H-H were located at 9.5 and 5.5 m, respectively, from the end wall of the excavation (Fig. 3). Because these sections were close to the corner, both sections could be affected by the corner effect of the excavation: the lateral wall deformation in these sections was expected to be smaller than that under plane strain conditions such as in Section E-E. Both the observed and predicted wall movements at Section H-H (Fig. 12a) were heavily influenced by the corner effect, as demonstrated by values smaller than those obtained from Section E-E (Fig. 11d). The predicted maximum wall displacement matched the measurement, indicating that the 3D FE model is capable of capturing the 3D corner effect of the excavation.

By contrast, the measured wall deformation in Section D-D was considerably larger than the predicted values for Section D-D (Fig. 12b) and the measured value in Section E-E, which was under plane strain conditions. This may be attributable to the presence of a large opening in the slab (see Fig. 2) for the launching of a tunnel boring machine (TBM), which can substantially reduce slab stiffness. However, this large opening on the slab was not considered in the numerical simulation. Further investigation is required to assess the influence of the size and location of a slab opening on the slab stiffness and wall deformation.

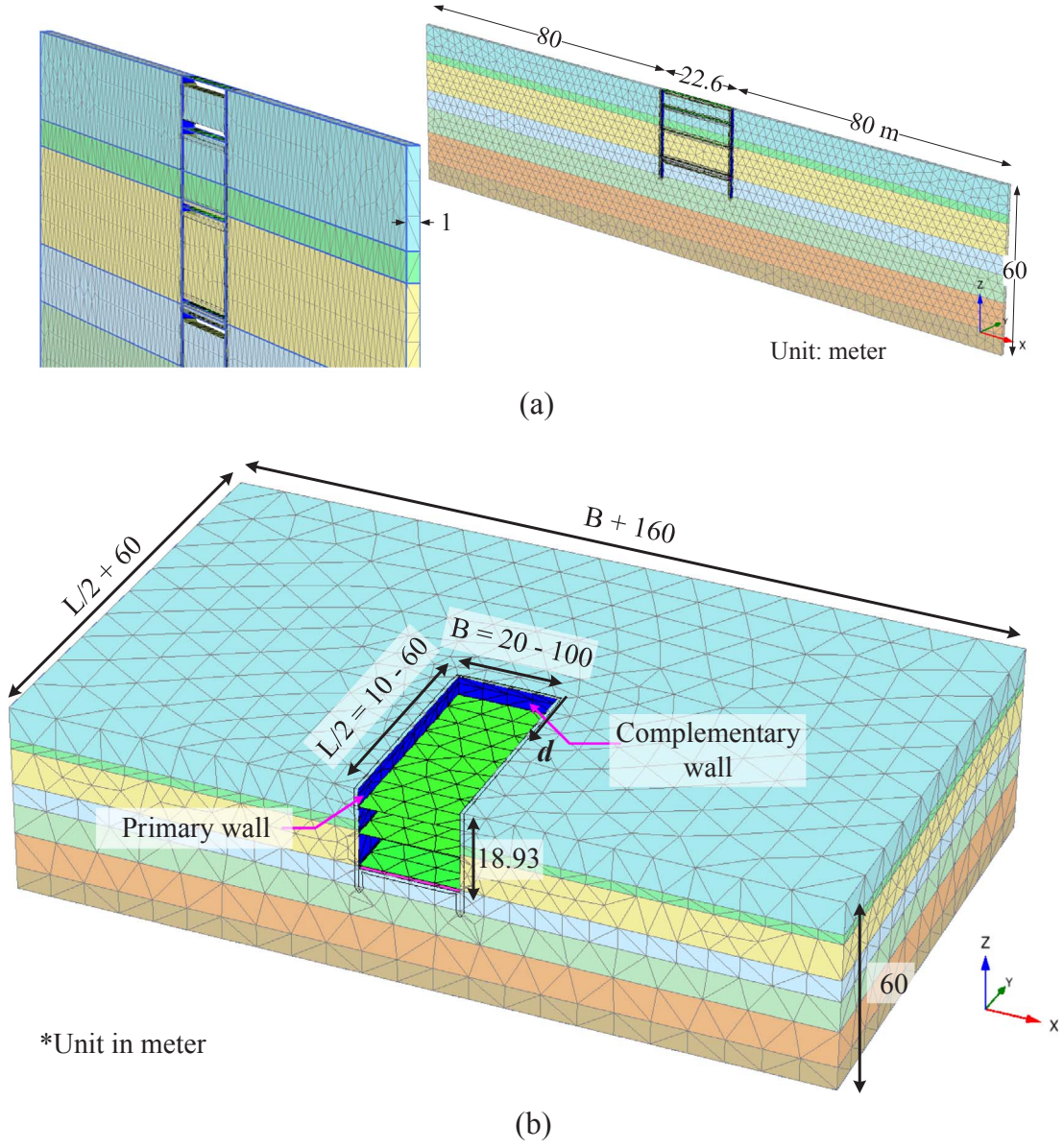

Fig. 13. 3D numerical model for determination of plane strain ratio: (a) unit length model; (b) 3D model for parametric study.

6. Parametric study of 3D effects

6.1. Plane strain ratio

After model verification, a series of parametric studies were performed to develop a PSR chart. The 3D effects on the wall deformation were quantitatively assessed using the PSR, which is the ratio of the maximum wall deformation of a section to its maximum wall deformation under plane strain conditions. This ratio was first proposed by Ou et al. (1996).

$$PSR = \frac{\delta_{hm,d}}{\delta_{hm,ps}} \tag{8}$$

where $\delta_{hm,d}$ is the maximum wall deformation at a certain section of the wall and $\delta_{hm,ps}$ is its maximum wall deformation under plane strain conditions. For engineering practice, the PSR chart provides an alternative for transferring the wall displacement from a 2D analysis to one that considers the 3D effects, which therefore provides designers with a practical reference to account for the 3D effects of excavations on wall deformations.

A 3D unit length model (Fig. 13a) was used to predict wall deformation under plane strain conditions. The 3D unit length model is similar to the 3D benchmark model (Fig. 10) in depth and width, but a 1-m length in the longitudinal direction was purposely established. The plane strain condition was further ensured by comparing the results of the unit length model with those of a 2D model. Fig. 14 shows the comparison of the wall deformation and wall bending moment between the 3D unit length model and 2D model. Comparison results revealed that the wall deformation and bending moment predicted from the both models were in good agreement, verifying that the 3D unit length model was under plane strain conditions. Hence, the output of the 3D unit length model was employed as the maximum wall movement under plane strain conditions.

A series of parametric studies were performed by varying the excavation length and width to evaluate the 3D effects of the excavation on the wall deformation. Fig. 13b shows the 3D model for the parametric studies used to develop the PSR chart. A 3D half-symmetric model, which was similar to the 3D benchmark model (Fig. 10), was considered for analysis. The length of the excavation ($L/2$) varied from 10 to 60 m and the width of the excavation (B) was between 20 and

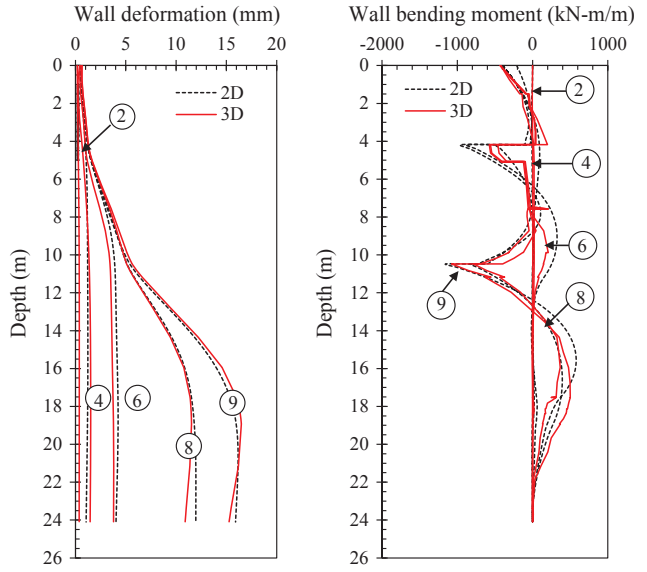

Fig. 14. Comparison of results from 2D plane strain model and 3D unit length model: (a) wall deformation; (b) wall bending moment. (Numbers in circles indicate the construction phases as indicated in Table 1).

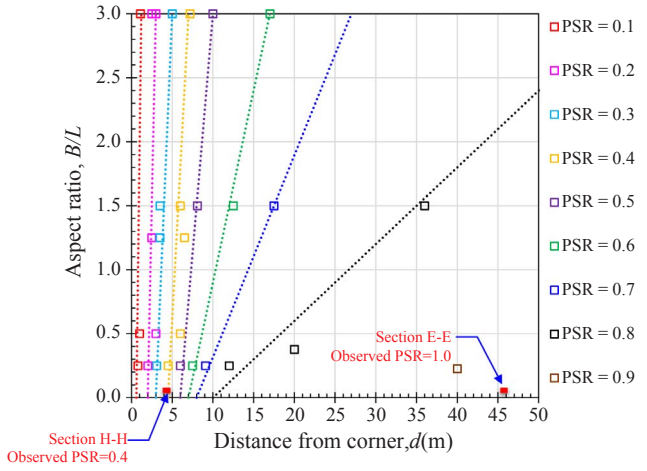

Fig. 15. PSR chart for Jakarta clay and comparison with observed PSR.

100 m. The remaining details were the same as those for the 3D model in the benchmark analysis.

Fig. 15 presents the PSR values for Jakarta clay corresponding to various values of distance from the corner (d) and aspect ratio (B/L). In general, for a given d, B/L has a considerable influence on the PSR. The displacements easily reach plane strain conditions in very narrow excavations (smaller B/L) but not in wide ones. For distances from the corner less than 10 m, the PSR value varied from 0.1 to 0.6. The influence of the corner effect decreased when d was greater than 30 m; the PSR value exceeds 0.7, regardless of the B/L. Under these conditions, the maximum wall deformation at a certain d was not substantially smaller than the maximum deformation under plane strain conditions, which suggested the decreasing influence of the 3D effect on the wall deformation.

The PSR values obtained from actual wall deformation in Sections E-E and H-H are also plotted on the PSR chart. Section E-E was considered to be under plane strain conditions because it was located far (approximately 60 m) from the corner. The distance from the corner for Section H-H was 5.5 m. According to the observation results, the PSR value for Section H-H was 0.39, and according to the numerical results, the PSR was 0.4. Therefore, the PSR chart developed in this study was in close agreement with the PSRs obtained from observations.

The PSR chart for Jakarta clay was further compared with that for Taipei clay (Ou et al., 1996), as shown in Figs. 16 and 17. The case reported by Ou et al. (1996) as a research background was an excavation constructed using the top-down method and retained by 1.1-m thick, 42-m deep reinforced concrete diaphragm wall. The maximum excavation depth was 20.3 m. The ground on site mainly consisted of very thick soft clay, occasionally with sand. Similar to the soil in Jakarta clay, the top 5 m soil layer had a very low SPT-N value between 2 and 7. The soil within the excavation depth typically had SPT-N values less than 11, which is considerably lower than those in Jakarta clay at a given depth. On the basis of SPT-N value comparison, the Jakarta clay was expected to be stiffer than the Taipei clay.

Fig. 16 compares the PSR values for two excavation cases at a fixed B/L ratio with various distances from the corner. In all B/L cases, the PSR increased gradually with an increase in distance from the corner. Additionally, the PSR value tended to increase as the B/L ratio decreased. For B/L ratios lower than 1.0, the PSR values of the two cases differed only slightly. Therefore, the ground condition did not substantially affect the PSR value when the dimensions of the excavation were narrow. Conversely, when the B/L was between 1.0 and 3.0, the PSR values from the different cases varied significantly. Fig. 17 shows an overall comparison of PSR charts for Jakarta and Taipei clay. In general, the PSR values in Jakarta clay are higher than those in Taipei clay for fixed B/L and d conditions. This observation indicates that stiff soil (Jakarta clay in this case) results in a high PSR value because of less wall deformation in stiff soil. This study revealed that, in addition to the geometry of the excavation, the soil stiffness affects the PSR value. Nevertheless, many other factors, including construction sequences, retaining wall systems, and soil shear strength, may also affect the 3D behavior of the excavation. Further investigation comparing the stress fields along the excavation is required for the detailed evaluation of the influence of these factors on PSR values.

6.2. Wall deflection path

The concept of the wall deflection path (WDP) proposed by Moh and Hwang (2005), Hwang and Moh (2007), Hsiung and Hwang (2009), and Hsiung et al. (2013) was adopted in this study to characterize the relationship between the maximum wall deformation and excavation depth during the excavation. The WDPs for Jakarta clay were developed according to the measured inclinometer readings from this excavation project. The WDP reference envelope for Taipei clay was also provided for comparison. The inflection point of the WDP reference envelope for Taipei clay was at a depth of 4 m because the first excavation depth was generally shallower than 4 m in construction practice in Taipei. The reference envelope was extended to a depth of 100 m to include the various depths of the final excavation level.

Fig. 18 shows the WDPs for Jakarta and Taipei clay. Because of the influence of the corner effect, the WDP of Section E-E was clearly larger than that of Section H-H at a given excavation depth. As explained previously, because of the influence of the slab opening, the WDP of Section D-D exhibited a larger maximum wall deformation at the final excavation depth than those of Sections E-E and H-H. Regardless of the wall section locations, the WDPs for Jakarta clay were consistently smaller than the reference envelope of WDP for Taipei clay. This is because less wall deformation occurs in stiff soil (Jakarta clay in this case), resulting in a smaller WDP. Similar to the PSR findings, the WDP was affected by both the 3D corner effect and the stiffness of the subsurface soil.

7. Conclusions

This paper presents a case study and numerical simulations for the 3D effects of a large-scale deep excavation on wall deformation in Central Jakarta, Indonesia. The geotechnical engineering properties of

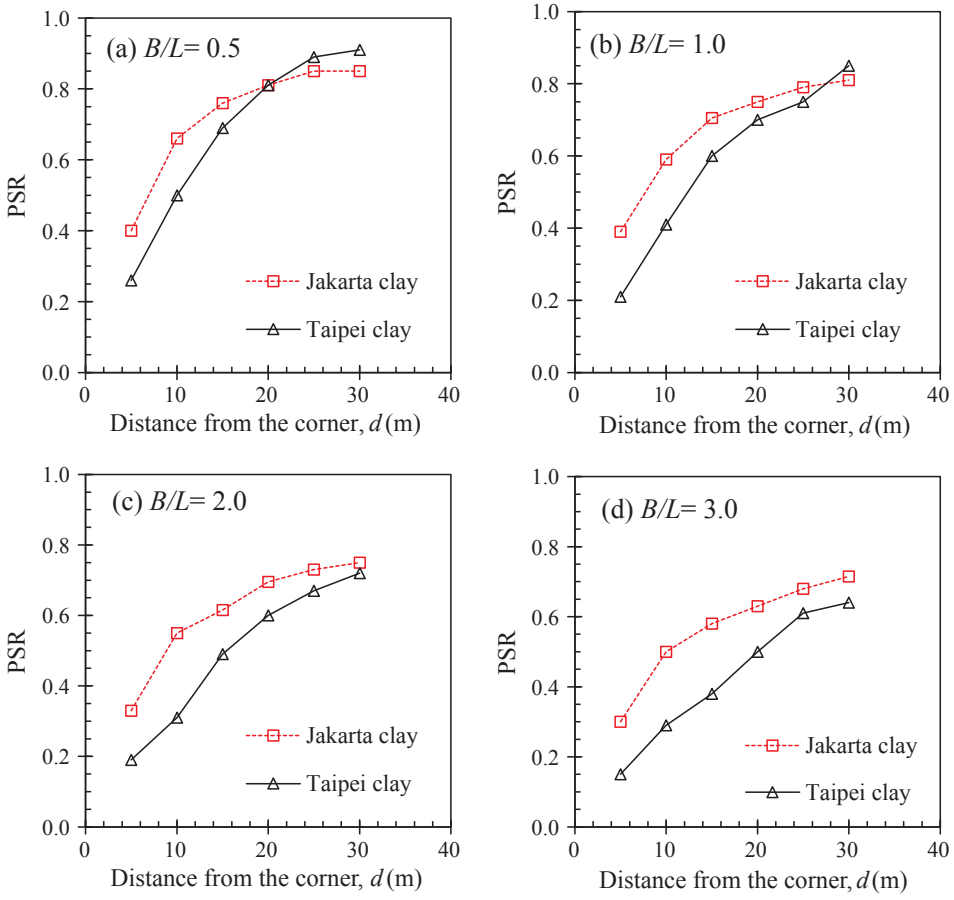

Fig. 16. Variation of PSR with d at various B/L =: (a) 0.5; (b) 1.0; (c) 2.0; (d) 3.0.

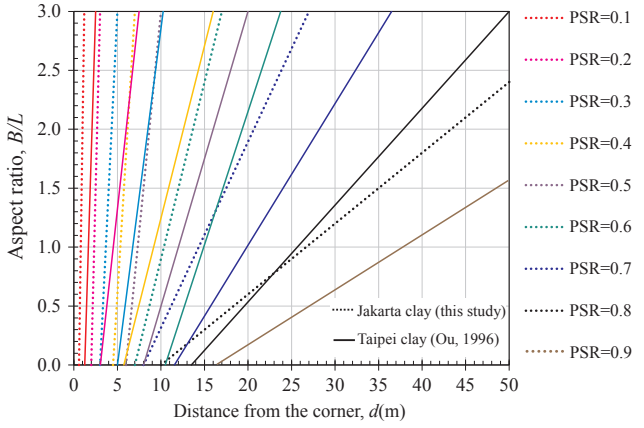

Fig. 17. Comparison of PSR charts for Jakarta and Taipei clay.

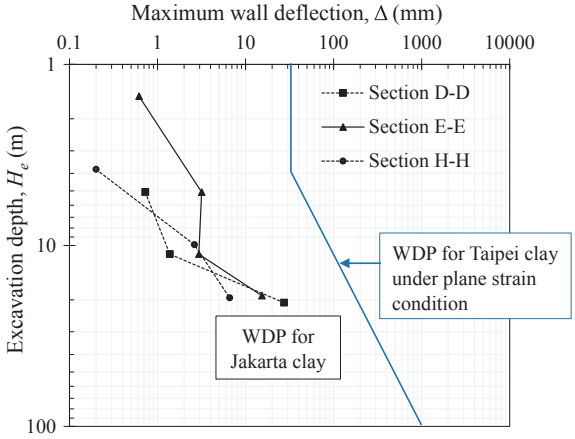

Fig. 18. Wall deflection paths (WDP) for Jakarta and Taipei clay.

soil (i.e., undrained shear strength and modulus) were established using data from a site investigation, in situ and laboratory tests, and empirical correlations with SPT-N. The performance of the 3D FE model for predicting the observed wall deformation influenced by the 3D corner effect was validated in this study. The PSR and WDP affected by the 3D corner effect were evaluated and discussed. The following conclusions were drawn from the results:

1. The subsurface soil profile of the construction site in Central Jakarta generally consisted of soft to firm AC overlying stiff to hard AC and DC. The natural water content of the clay ranged from 28.19% to 89.26% with a calculated LI of between 0.05 and 0.65. The SPT-N values were generally low (less than 8) to a depth of 8 m, but they increased to 30 at a depth of 15 m.
2. For soil in Central Jakarta, a linear relationship between the soil modulus (obtained from in situ PMT) and depth was established as $E_{50} = 833\ (z + 76)$, where E_{50} and z were measured in kilopascals and meters, respectively. The numerical results indicated that the HS model with the soil modulus obtained from in situ PMT yielded reasonable predictions for the excavation-induced wall deformation.
3. The 3D corner effect on wall deformation was observed through field measurement by using inclinometers and through numerical prediction using 3D FE analysis. Because Section H-H was close to the corner of the excavation, the wall deformation was considerably smaller than that in Section E-E, which was under plane strain conditions Although Section D-D was also close to the corner of the excavation, a large wall deformation was observed, resulting from

the influence of a large opening on the slab for TBM launching, which significantly reduced the stiffness of the slab and increased the wall deformation.

4. The 2D plane strain and 3D unit length analyses were compared. The wall deformation and bending moment predicted by the 2D and 3D analyses were in close agreement, confirming that the results from the 3D unit length analysis reflected plane strain conditions.
5. On the basis of the parametric study, the PSR was determined for the excavations in Jakarta clay. The PSR increased gradually as the distance from the corner increased and the B/L ratio decreased. In general, the PSR values in Jakarta clay are higher than those in Taipei clay at fixed B/L and d conditions because Jakarta clay is stiffer than Taipei clay. This study revealed that the PSR value was influenced by not only the 3D corner effect but also the stiffness of the subsurface soil.
6. The WDPs from inclinometer readings at various sections along the excavation were drawn and compared. The WDP was also affected by the 3D corner effect and soil modulus.

References

Architectural Institute of Japan, 2001. Recommendations of Design of Building Foundation. Japan (in Japanese).

Calvello, N., Finno, R., 2004. Selecting parameters to optimize in model calibration by inverse analysis. Comput. Geotechn. 31, 410–424.

Clough, G.W., O'Rourke, T.D., 1990. Construction-induced movements of in situ walls, design and performance of earth retaining structures. ASCE. Geotechn. Spec. Publ. 25, 439–470.

Finno, R.J., Arboleda-Monsalve, L.G., Sarabia, F., 2015. Observed performance of the One Museum park west excavation. J. Geotechn. Geoenviron. Eng. 141 (1), 04014078.

Gebreselassie, H., Kempfert, G., 2005. Sensitive study of the hardening soil model parameters based on idealized excavation. In: Proceedings of 11th International conference on computer methods and advances in geomechanics, Torino, Italy, pp. 321–328.

Hettiarachchi, H., Brown, T., 2009. Use of SPT blow counts to estimate shear strength properties of soils: energy balance approach. J. Geotechn. Geoenviron. Eng. 135 (6), 830–834.

Houston, W.N., Mitchell, J.K., 1969. Property interrelationships in sensitive clays. ASCE. J. Soil Mech. Found. Divis. 95 (4), 1037–1062.

Hsieh, P.G., Ou, C.Y., Lin, Y.K., Lu, F.C., 2015. Lessons learned in design of an excavation with the installation of buttress walls. J. GeoEng. 10, 67–73.

Hsiung, B.C.B., 2009. A case study on the behaviour of a deep excavation in sand. Comput. Geotechn. 36, 665–675.

Hsiung, B.C.B., Hwang, R.N., 2009. Evaluating Performance of Diaphragm Walls by Wall Deflection Path. SEAGS. Special Issue on Excavation and Tunneling in Geotechnical Engineering, pp. 81–90.

Hsiung, B.C.B., Wang, C.L., Lin, H.T., Chen, C.H., 2013. Design and performance of a large scale excavation adjacent to sensitive structures in urban area. In: Proceedings of the 2nd International Conference on Geotechnics for Sustainable Development-Geotec. Hanoi 2013, Hanoi, Vietnam.

Hsiung, B.C.B., Yang, K.H., Aila, W., Hung, C., 2016. Three-dimensional effects of a deep excavation on wall deflections in loose to medium dense sands. Comput. Geotechn. 80, 138–151.

Hwang, R.N., Moh, Z.C., 2007. Deflection paths and reference envelopes for diaphragm walls in the Taipei Basin. J. GeoEng. 1, 1–12.

Jaky, J., 1944. The coefficient of earth pressure at rest. J. Soc. Hungarian Archit. Eng. Budapest Hungry 355–358.

Khoiri, M., Ou, C.Y., 2013. Evaluation of deformation parameter for deep excavation in sand through case histories. Comput. Geotechn. 47, 57–67.

Kulhawy, F.H., Mayne, P.W., 1990. Manual on Estimating Soil Properties for Foundation Design. Electric Power Research Institute, Palo Alto, California.

Kung, G.T., Juang, C.H., Hsiao, E.C., Hashash, Y.M., 2007. Simplified model for wall deflection and ground-surface settlement caused by braced excavation in clays. J. Geotechn. Geoenviron. Eng. 133 (6), 731–747.

Lim, A., Ou, C.Y., Hsieh, P.G., 2010. Evaluation of clay constitutive models for analysis of deep excavation under undrained conditions. J. GeoEng. 5, 9–20.

Lin, D.G., Woo, S.M., 2007. Three-dimensional analyses of deep excavation in Taipei 101 construction project. J. GeoEng. 2, 29–41.

Likitlersuang, S., Surarak, C., Wanatowski, D., Oh, E., Balasubramaniam, A., 2013. Finite element analysis of a deep excavation: A case study from the Bangkok MRT. Soils Foundat. 53 (5), 756–773.

Mayne, P., Kulhawy, F.H., 1982. K_o-OCR relationships in soil. J. Geotechn. Eng. Divis. 108 (GT6), 851–872.

Moh, Z.C., Hwang, R.N., 2005. Geotechnical considerations in the design and construction of subways in urban areas. Seminar on recent developments on mitigation of natural disasters, urban transportation and construction industry, Jakarta, Indonesia.

Muir-Wood, A., 1983. Index properties and critical state soil mechanics. Paper presented at the Proceeding of the Symposium on Recent Developments in Laboratory and Field Tests and Analysis of Geotechnical Problems, Bangkok, Thailand.

Orazalin, Z., Whittle, A.J., Olsen, M.B., 2015. Three-dimension analysis of excavation support system for the Stata Centre Basement on the MIT campus. J. Geotechn. Geoenviron. Eng. 141 (7), 0501500.

Ou, C.Y., Chiou, D.C., Wu, T.S., 1996. Three-dimensional finite element analysis of deep excavations. J. Geotechn. Eng. 122 (5), 337–345.

Ou, C.Y., Shiau, B.Y., Wang, I.W., 2000. Three-dimensional deformation behavior of the Taipei national enterprise center (TNEC) excavation case history. Canad. Geotechn. J. 37 (2), 438–448.

Ou, C.Y., 2006. Deep Excavation: Theory and Practice. Taylor & Francis, Netherlands.

Schweiger, H.F., 2009. Influence of constitutive model and EC7 design approach in FEM analysis of deep excavations. In: Proceedings of ISSMGE International Seminar on Deep Excavations and Retaining Structures, Budapest, Hungary, pp. 99–114.

Surarak, C., Likitlersuang, S., Wanatowski, D., Balasubramaniam, A., Oh, E., Guan, H., 2012. Stiffness and strength parameters for hardening soil model of soil and stiff Bangkok clays. Soils Foundat. 52 (4), 682–697.

Wang, J.H., Xu, Z.H., Wang, W.D., 2010. Wall and ground movements due to deep excavations in Shanghai soft soils. J. Geotechn. Geoenviron. Eng. 136, 985–994.

Yong, K.Y., 2015. Learning lessons from the construction of Singapore Downtown line (DTL). In: Proceedings of International Conference and Exhibition on Tunneling and Underground Space, Kuala Lumpur, Malaysia.